Experimental and density-functional study of the electronic structure of $In_4Sn_3O_{12}$

D. H. O'Neil,[1,*] A. Walsh,[2] R. M. J. Jacobs,[3] V. L. Kuznetsov,[1] R. G. Egdell,[1] and P. P. Edwards[1]
[1]*Inorganic Chemistry Laboratory, Department of Chemistry, University of Oxford, South Parks Road, Oxford OX1 3QR, United Kingdom*
[2]*Materials Chemistry, Department of Chemistry, University College London, 3rd Floor, Kathleen Lonsdale Building, Gower Street, London WC1E 6BT, United Kingdom*
[3]*Chemistry Research Laboratory, Department of Chemistry, University of Oxford, Mansfield Road, Oxford OX1 3TA, United Kingdom*
(Received 23 July 2009; revised manuscript received 20 November 2009; published 12 February 2010)

The electronic structure of $In_4Sn_3O_{12}$ has been studied by optical and x-ray photoemission spectroscopies and has been compared to electronic structure calculations carried out using density-functional theory. An excellent agreement is found between the experimental valence-band structure and that predicted by the calculations. The valence band derives its dominant character from O $2p$ states with three distinct features emerging from the hybridization with In and Sn $5s$, $5p$, and $4d$ states, respectively. The position of the valence-band edge in the x-ray photoemission spectrum suggests a fundamental electronic gap of 2.7 eV whereas the onset of strong optical absorption is predicted to occur at 3.3 eV.

DOI: 10.1103/PhysRevB.81.085110 PACS number(s): 79.60.Bm, 71.15.Mb, 71.20.Nr, 78.20.Ci

I. INTRODUCTION

The *n*-type doped oxides of indium, tin, and zinc form the basis of a remarkable class of compounds referred to as the transparent conducting oxides (TCO). These materials offer the rare combination of high electrical conductivity with optical transparency over the visible wavelengths. In_2O_3 is arguably the prototypical TCO and tin-doped indium oxide (also known as indium-tin-oxide or ITO) finds widespread applications in electroluminescent devices, flat panel displays, and photovoltaic cells.[1,2] With increased technological demand for these applications and the escalating cost of indium, the development and optimization of new materials for transparent electrode applications represents one of the major challenges in materials science. However, several In_2O_3-based, multicomponent oxides are emerging with properties potentially suitable for specialized applications.[3]

Although the conductivity of $In_4Sn_3O_{12}$ in the bulk phase[4] is an order of magnitude lower than ceramic ITO,[5] the material remains a promising candidate to replace conventional ITO in transparent electrode applications. Several reports suggest that the conductivity of $In_4Sn_3O_{12}$ as a thin film is of the same order as traditional ITO films while maintaining significant optical transparency.[6] From an industrial perspective, the material $In_4Sn_3O_{12}$ can offer comparable conductivity and transparency over the visible spectrum to ITO whist having a lower percentage of indium and would require minimal changes to existing deposition equipment. The net result is a significantly lower materials cost.

The crystal structure of $In_4Sn_3O_{12}$ is based on a rhombohedral unit cell (space group: $R\bar{3}H$) with lattice parameters $a=6.2071$ Å and $\alpha=99.29°$.[7] This structure is most easily viewed in a hexagonal basis, with lattice parameters $a=9.4604$ Å and $c=8.8584$ Å.[7] Within the unit cell, there are two nonequivalent cation sites; the six coordinate $3a$ position (a distorted cube with anion vacancies on a pair of opposite vertices) and a general $18f$ position (sevenfold coordination with anions sets at the corners of a highly distorted cube with a vacancy at one vertex).[7] In $In_4Sn_3O_{12}$ the $3a$ positions are exclusively occupied by the Sn cations, while the $18f$ positions are occupied by both Sn $(\frac{1}{3})$ and In $(\frac{1}{3})$ cations which form three planes along the *c* axis of the unit cell as shown in Fig. 1. Choisnet *et al.*[8] have identified several transparent conductors, including In_5SnSbO_{12} and $In_{5.5}Sb_{1.5}O_{12}$, that exist as part of a Sb-substituted solid solution derived from $In_4Sn_3O_{12}$. First-principles band-structure calculations performed by Ren *et al.*[9] demonstrate strong similarities between the electronic structures of $In_4Sn_3O_{12}$ and In_5SnSbO_{12} suggesting comparable electronic and optical properties in these materials.

While the crystallographic structure of $In_4Sn_3O_{12}$ has been published,[7] to our knowledge the electronic structure has not been investigated experimentally. In this paper, we investigate the electronic structure of $In_4Sn_3O_{12}$ with x-ray photoemission and optical spectroscopies and compare our findings with density-functional theory (DFT) calculations. We find that the fundamental gap of $In_4Sn_3O_{12}$ occurs nearly 0.6 eV below the onset of strong optical absorption in a manner that resembles In_2O_3.[10]

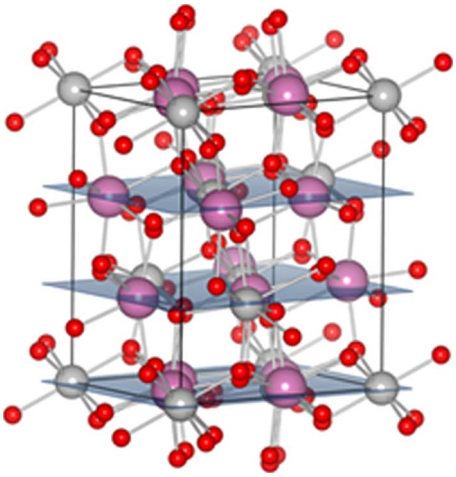

FIG. 1. (Color online) The crystal structure of $In_4Sn_3O_{12}$ with In, Sn, and O shown as large, medium, and small spheres, respectively. The three cationic planes that exist along the *c* axis of the unit cell are shaded.

II. EXPERIMENTAL

Thin films of composition $In_4Sn_3O_{12}$ were deposited onto 1 cm^2 glass substrates held at a temperature of 500 °C to a thickness of between 800–900 nm by pulsed laser deposition using a KrF excimer laser (Lambda Physik, Complex 102, $\lambda = 248$ nm) in the department of Metallurgy and Materials, University of Birmingham. The diffraction pattern of the films measured in a θ-2θ diffractometer displayed only reflections associated with the rhombohedral $R\bar{3}H$ structure. Single field Hall measurements indicated a carrier concentration of 4.62×10^{20} cm^{-3} and a mobility of 30.6 $cm^2\ V^{-1}\ s^{-1}$ for this film.

High-resolution x-ray photoemission spectra were recorded using a Scienta ESCA 300 spectrometer. This setup incorporates a rotating anode Al $K\alpha$ ($h\nu = 1486.6$ eV) x-ray source, a seven crystal x-ray monochromator, and a 300 mm mean radius spherical sector electron-energy analyzer with parallel electron-detection system. The x-ray source was operated with a 200 mA emission current and a 14 kV anode bias, while the analyzer operated at a pass energy of 150 eV with 0.8 mm slits. The Gaussian convolution of the analyzer resolution with the intrinsic linewidth of the x-ray source (260 meV) gives an effective instrument resolution of 400 meV. Binding energies were measured related to the Fermi level of a silver sample regularly used to calibrate the spectrometer.

Transmission measurements were made using a Cary 5000 UV-Visible-NIR spectrophotometer over wavelengths between 200 and 2500 nm. Thin-film samples were mounted in sample holders specifically designed for transmission measurements in the Cary 5000 spectrophotometer. An aperture mask of 1 mm was used to collimate the beam. The dielectric function was extracted from the optical data using the software program WVASE.[11]

A digital instruments multimode atomic force microscope (AFM) was used with a Nanoscope IIIa controller, operating in tapping mode with an "E" scanner, having a lateral range of 12 μm and a vertical range of 3.5 μm. Silicon probes (Nascatec GmbH model NST-NCHFR), with resonant frequencies of approximately 320 kHz were used. X, Y, and Z calibrations of the microscope was accomplished by scanning both a 1 μm Scribed Gold Calibration grid and a 10 μm pitch 200 nm three-dimensional reference from digital instruments. An atomic force micrograph of a representative $In_4Sn_3O_{12}$ film is shown in Fig. 2 and clearly shows the presence of a very rough surface and granular region. The typical lateral dimension of the grains is in the range 100–200 nm. The height scale in the 3×3 μm^2 area image extends over about 10 nm although due to finite-tip-size effects it is quite probable that the rough-surface region extends to a greater depth.

III. THEORETICAL METHODS

The first-principles electronic structure of $In_4Sn_3O_{12}$ was calculated using DFT, as implemented in the VASP code.[12,13] Exchange-correlation effects were treated within the generalized gradient approximation (Perdew-Burke-Ernzerhof functional).[14] A plane-wave basis set was employed (500 eV kinetic-energy threshold) with dense k-point sampling ($5 \times 5 \times 5$ mesh). The In and Sn $4d$ (Ref. 10) states were treated as valence, with the projector augmented wave method used to represent the core electrons.[15] The optical absorption spectrum was calculated from direct valence to conduction-band optical transitions using the ground-state all-electron wave functions,[16,17] which excludes indirect (phonon-assisted) transitions. The partial density of states (DOS) were obtained from site projection of the wave functions onto spherical harmonics.

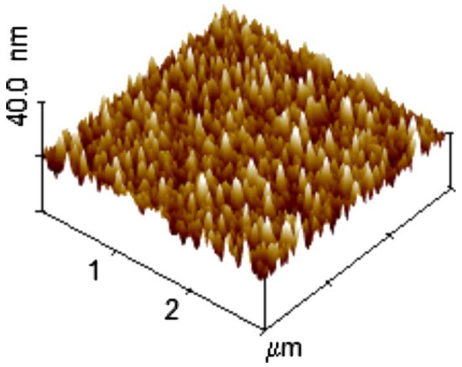

FIG. 2. (Color online) Atomic force micrograph of a 3×3 μm^2 region of the surface of an $In_4Sn_3O_{12}$ film deposited on glass substrate at a temperature of 500 °C.

The hexagonal unit cell of $In_4Sn_3O_{12}$, containing 57 atoms (or 3 f.u.),[7] was used for the calculations. A random occupation of the 18f cation sites, which form three planes along the c axis of the unit cell, was assumed, with the presence of two Sn and four In ions on each layer. While a lower energy configuration may be obtained using a larger supercell, the effects on the electronic structure are expected to be small. The internal positions were relaxed to below 0.005 eV $Å^{-1}$ using a conjugate-gradient minimization scheme.

IV. RESULTS AND DISCUSSION

A. Electronic structure

Figure 3 shows the band structure of $In_4Sn_3O_{12}$ along the high-symmetry directions of the Brillouin zone. The first conduction band consists of a single broad s-type band with its minimum centered at the Γ point. The conduction-band minimum (CBM) lies relatively low in energy compared to the average energy of the band edge across the Brillouin zone, as a result of the large size and electronegativity mismatch between anion and cation. This indicates a potentially high dopability for $In_4Sn_3O_{12}$ as well as a small effective mass. The effective mass at the CBM is calculated as $0.18m_e$, which is slightly larger than that of In_2O_3 ($\sim 0.15m_e$).[18]

The valence-band maximum (VBM) occurs also at the Γ point and thus $In_4Sn_3O_{12}$ is predicted to be a direct gap material with an energy gap of 1.2 eV. It is also evident that there is a large separation between the first and second conduction bands at the Γ point, preventing optical transitions within the conduction band and improving the overall transparency. Thus, it appears that the band structure of $In_4Sn_3O_{12}$

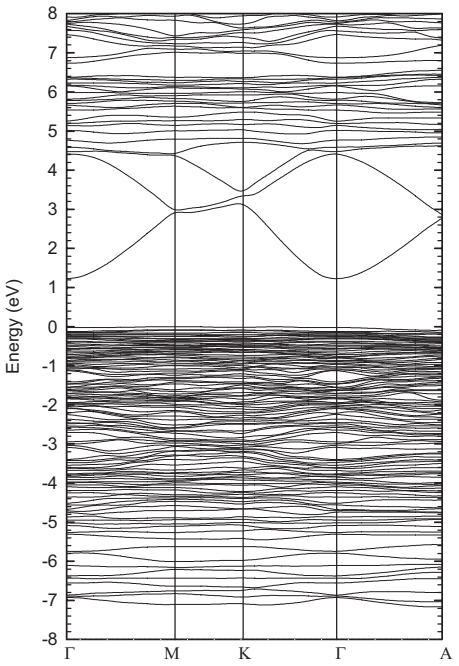

FIG. 3. The electronic band structure of $In_4Sn_3O_{12}$ along the high-symmetry directions of the Brillouin zone. The valence-band maximum is set at 0 eV.

displays many of the electronic features responsible for the high conductivity and transparency found in In_2O_3.

In Fig. 4 we plot the calculated total and partial (ion and angular momentum decomposed) electronic DOS for

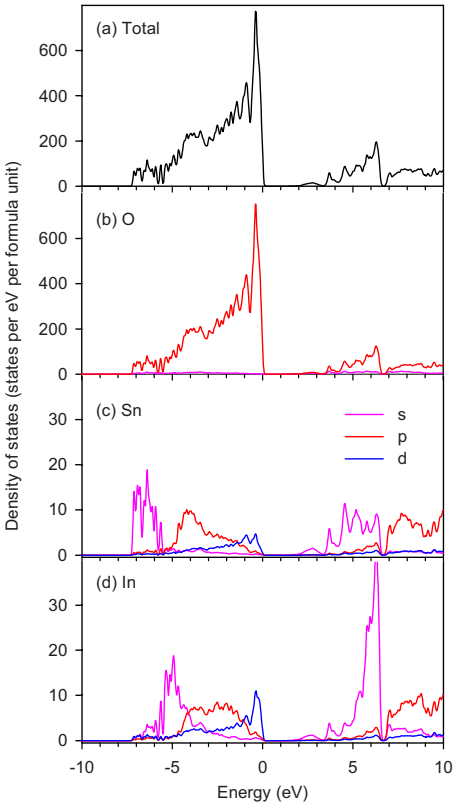

FIG. 4. (Color online) The electronic DOS for $In_4Sn_3O_{12}$; (a) total DOS and ion-decomposed DOS (b) O, (c) Sn, and (d) In.

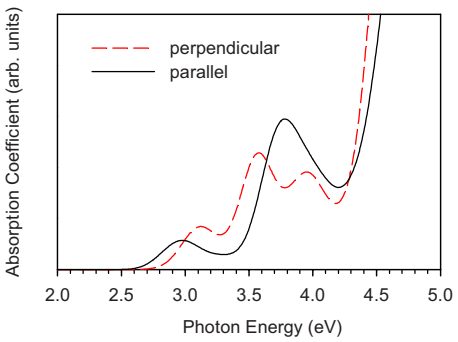

FIG. 5. (Color online) The calculated optical absorption coefficient of $In_4Sn_3O_{12}$ as a function of photon energy. The components parallel and perpendicular to the hexagonal c axis are shown as solid and dashed (red online) lines, respectively. The absorption profiles have been rigidly shifted by +1.5 eV to account for the discrepancy between the calculated band gap and the band gap determined by photoemission spectroscopy (see text).

$In_4Sn_3O_{12}$. The valence band derives its overall character from O $2p$ states, with increasing contributions from the metal $4d$ states as it approaches the VBM. We find that the top of the valence band consists predominantly of the In $4d$ and O $2p$ states which hybridize strongly, whereas the bottom of the conduction band arises mostly from the admixture of oxygen and cation s states. Two distinct features emerge in the total density of states resulting from the hybridization of the O $2p$ states with In and Sn $5p$ (∼−5 eV) and $5s$ (∼−7 eV) states, respectively.

In Fig. 5 we show the calculated optical absorption spectrum for $In_4Sn_3O_{12}$ resolved into its components parallel and perpendicular to the hexagonal c axis. DFT calculations, using semilocal functionals such as PBE, invariably underestimate the separation between conduction and valence bands and we have applied a rigid correction of 1.5 eV to match the calculated band gap with the energy gap determined experimentally by photoemission measurements (see below). The correction is very close to that required (1.4 eV) to reconcile the optical absorption spectrum of In_2O_3 at the same level of theory.[10] We find that the direct optical transitions between the band edges for $In_4Sn_3O_{12}$ at the Γ point are not formally forbidden as is the case for In_2O_3 (Ref. 10) but nonetheless transitions at the band edge have very low dipole intensity. The weak optical onset at 2.7 eV is followed by a set of weak transitions occurring from states approximately 0.4 eV below the VBM before the onset of stronger optical transitions from states even deeper in the valence band. The build up of intensity in the optical spectrum correlates with increasing metal $5p$ character in the valence-band states from which the transitions derive. The rapid increase in the calculated absorption coefficient approximately 0.7 eV above the energy of the fundamental gap is consistent with a direct allowed gap of 3.3 eV determined from the optical measurements on $In_4Sn_3O_{12}$ films, as will be discussed below.

B. Optical spectra

The optical transmission spectrum of an $In_4Sn_3O_{12}$ film is shown in Fig. 6(a). The decrease in optical transmission at

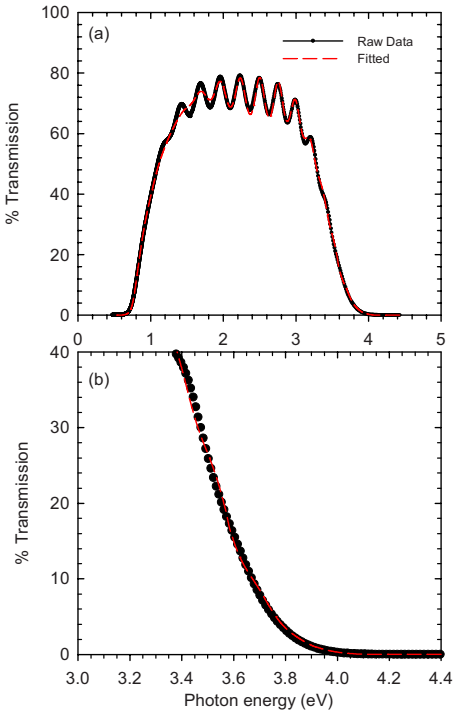

FIG. 6. (Color online) (a) Optical transmission data for an $In_4Sn_3O_{12}$ film. The raw data are shown as a solid line with the simulation shown as a dashed line (red) and (b) expansion of the high-energy spectrum showing the close fit of optical model to the raw data around the band edge.

high energy corresponds to the onset of dipole allowed interband absorption across the optical gap of the material. A decrease in transmission is also apparent at the low energy end of spectrum and is associated with increasing reflectivity when the photon energy falls below the plasma energy of the conduction electrons. Between these two extremes, there is a region of high transmittance with a series of oscillations that are the result of optical interference. Similar data have been obtained in a number of related materials such as Al-doped ZnO (Ref. 19) and Sn-doped In_2O_3.[20] As discussed recently by Borondics *et al.*[21] it is possible to use transmittance data to derive the real and imaginary parts of the complex dielectric function. This may be achieved either by applying a Kramers-Kronig transformation to obtain an energy-dependent phase shift direct from the experimental transmittance data[21] or by introducing a model dielectric function that satisfies the Kramers-Kronig relationships. We preferred the latter approach as the direct approach formally requires an integration of transmittance data across an infinite range of energies. Experimentally of course we have transmittance measurements in a restricted spectral range. The optical transmittance data of Fig. 6(a) were therefore fitted to a model dielectric function $\varepsilon(E)$ which includes a Drude term $\varepsilon_D(E)$ to account for the plasma oscillations of the conduction electron gas as well as a Lorentzian oscillator $\varepsilon_L(E)$ to account for interband excitations around the band edge. The model also introduces a high-frequency background dielectric constant $\varepsilon(\infty)$ which deals with contributions to the polarizability of the system arising from electronic excitations at energies well above that of the band gap. A simple model

TABLE I. Parameters extracted from the modeling of the transmittance of $In_4Sn_3O_{12}$ deposited at 500 °C and under a 7.5 mTorr pressure of oxygen using the dielectric function described in Eqs. (1)–(3). The errors of the extracted parameters show 90% confidence limits and the final fitting quality is shown by the value of χ^2.

Fitting parameters	$In_4Sn_3O_{12}$ film
d_{TCO} (nm)	799 ± 3
d_{SUR} (nm)	167 ± 1
A_D (eV)	1.553 ± 0.001
Γ_D (eV)	0.116 ± 0.001
A_L (eV)	13.68 ± 0.01
Γ_L (eV)	2.36 ± 0.02
E_L (eV)	6.45 ± 0.04
$\varepsilon(\infty)$	1.25 ± 0.13
χ^2	0.939

of this sort has been shown to provide a robust basis for analyzing optical or energy-loss spectra of metallic oxides.[22] We thus have

$$\varepsilon(E) = \varepsilon(\infty) + \varepsilon_L(E) + \varepsilon_D(E), \tag{1}$$

where

$$\varepsilon_L(E) = \frac{A_L^2}{E_L^2 - E^2 - i\Gamma_L E} \tag{2}$$

and

$$\varepsilon_D(E) = -\frac{A_D^2}{E^2 + i\Gamma_D E}. \tag{3}$$

Here E_L, A_L, and Γ_L represent the transverse resonance energy, amplitude and broadening parameter, respectively, of the interband oscillator and A_D and Γ_D are the amplitude and broadening parameters for the plasmon. The film itself was considered to consist of two layers; a bulk TCO layer and a surface roughness layer that corresponds to a 50/50 vol. % mixture of the bulk TCO layer and void space. The thickness of the bulk TCO layer and the surface roughness layer were found to be 799 ± 3 nm and 167 ± 1 nm, respectively. The need for a roughness layer is compatible with the AFM image presented in Fig. 2. The parameters used to model the spectral transmission data of the $In_4Sn_3O_{12}$ film are given in Table I and the fitted profile is superimposed on the experimental data in Fig. 6(a). The fit is seen to be very good, especially in the region of the band-gap cutoff, which is shown in greater detail in Fig. 6(b). The simple three parameter Lorentzian oscillator model is preferable to the more complicated four parameter Tauc-Lorentzian model that has become popular in recent years for description of the band-edge region in transparent conductors and related materials.[23,24] This is because the Tauc function introduces an abrupt cutoff below a critical band-gap energy and cannot include effects due to Urbach tailing and weak transitions below the direct fully allowed gap that are found in the present work.

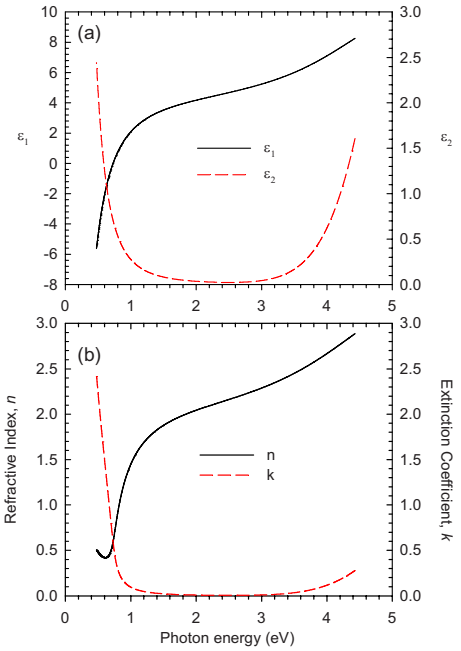

FIG. 7. (a) (Color online) Variation of the complex dielectric function $\varepsilon=\varepsilon_1+i\varepsilon_2$ with photon energy for an $In_4Sn_3O_{12}$ film. The plasma frequency is defined by the photon energy where $\varepsilon_1(E)=0$. (b) Variations in refractive index (n) and extinction coefficient (k) with photon energy for the $In_4Sn_3O_{12}$ film obtained from the dielectric functions.

In Fig. 7 we show the variations in the real and imaginary parts of the dielectric function with photon energy for the $In_4Sn_3O_{12}$ film. In addition we show the corresponding variations of the refractive index and extinction coefficient as a function of wavelength. The increase in ε_2 (and consequently k) at the low-energy end of the spectrum indicates losses due to conduction-electron excitation. At sufficiently low energy, the contribution of the interband oscillator to the dielectric function assumes an essentially constant value and hence the real part of dielectric constant can be expressed as

$$\varepsilon_1(E) \approx \varepsilon'(\infty) - \left(\frac{A_D^2}{E^2+\Gamma_D^2}\right). \tag{4}$$

$\varepsilon'(\infty)$ is greater than $\varepsilon(\infty)$ appearing in Eq. (1) owing to the contribution of the interband oscillator to the background polarizability. In Fig. 8 we show the linear relationship between ε_1 and $1/(E^2+\Gamma_D^2)$ over a wide energy range that indicates the validity of the Drude theory for this material. The background dielectric constant $\varepsilon'(\infty)$ relevant to the plasmon oscillation was determined for the material $In_4Sn_3O_{12}$ as 4.57 from the intercept of $1/(E^2+\Gamma_D^2)$ with the ε axis. Within the Drude model, the amplitude (A_D) is related to the plasma frequency ($\hbar\omega_p$) by the expression

$$A_D^2 = \varepsilon_\infty(\hbar\omega_p)^2, \tag{5}$$

where the plasma frequency can be further expressed as

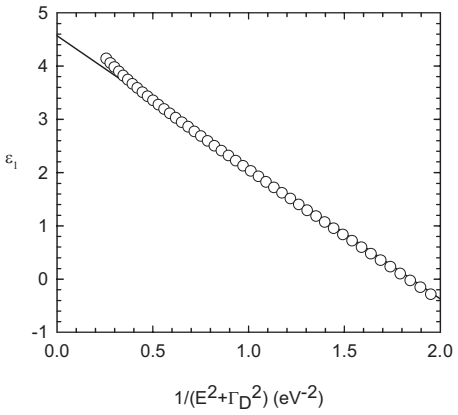

FIG. 8. Real part of the dielectric function of the $In_4Sn_3O_{12}$ film plotted as a function of $1/(E^2+\Gamma_D^2)$. The background dielectric constant $\varepsilon'(\infty)$ is determined by a linear extrapolation (solid line) to the intercept at $1/(E^2+\Gamma_D^2)=0$.

$$\hbar\omega_p = \hbar\left[\frac{ne^2}{\varepsilon_\infty\varepsilon_0 m^*}\right]^{1/2}. \tag{6}$$

Here n is the carrier concentration, e is the electronic charge, ε_0 is the permittivity of free space, and m^* is the effective mass. A value of $\hbar\omega_p=0.73$ eV was obtained from the amplitude of the Drude oscillator and the high-frequency dielectric constant. Using the value of 4.62×10^{20} cm^{-3} for the carrier concentration as determined from the Hall measurements, we obtain a value of $0.26m_e$ for the effective mass of electrons in $In_4Sn_3O_{12}$. This is greater than the value derived from the band-structure calculations. However, it should be noted that the effective mass that determines the plasma energy is the effective mass at the Fermi level.[25] Due to nonparabolicity the effective mass increases as the Fermi level moves upward within the conduction band. Thus the value of $0.26m_e$ is in tolerable agreement with the value of effective mass determined from the DFT calculations above. From the bulk carrier concentration and effective mass, the position of the Fermi level with respect to the conduction-band minimum, is calculated from a simple free-electron model

$$E_F = \frac{\hbar^2}{2m^*}[3\pi^2 n]^{2/3}. \tag{7}$$

Therefore in the bulk material, the Fermi level lies 0.85 eV above the conduction-band minimum.

At high energy the increase in ε_2 indicates the onset of allowed optical interband absorption. The absorption coefficient (α), which is derived from the extinction coefficient through $\alpha=4\pi k/\lambda$, is related to the electronic gap of a direct semiconductor by the relationship[26]

$$\alpha h\nu = \alpha_0[h\nu - E]^{1/2}. \tag{8}$$

Here α_0 is a constant, ν is the frequency of incident radiation, and E is the direct energy gap. In Fig. 9 we show a plot of $(\alpha h\nu)^2$ derived from the optical measurements of the thin film against photon energy $h\nu$ and compare this to the analogous plot of the mean-absorption coefficient determined from the DFT calculations. The allowed direct optical gap

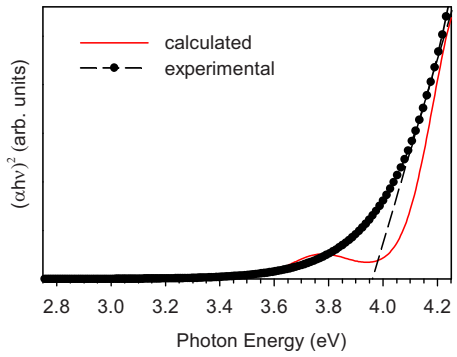

FIG. 9. (Color online) Square of the absorption coefficient $(\alpha h\nu)^2$ as a function of photon energy for an $In_4Sn_3O_{12}$ film (data points). The direct allowed optical band gap was determined from the linear extrapolation of the experimental data and is shown as a dashed line. The value of $(\alpha h\nu)^2$ extracted from the DFT calculations is shown for comparison as a solid line (red). These calculated data have been shifted by $E_F - E_R = 0.67$ eV (see text) as compared with Fig. 5 to allow for the shift in the position of the Fermi level relative to the top of the valence band due to degenerate doping.

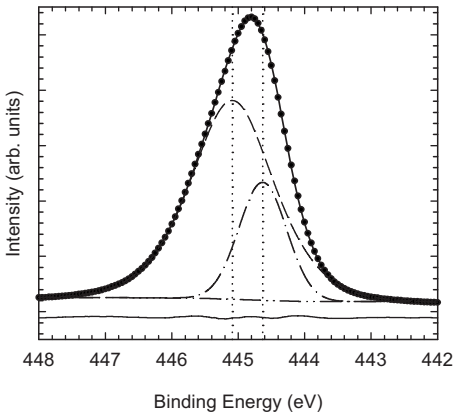

FIG. 10. In $3d_{5/2}$ core-level photoelectron spectrum of an $In_4Sn_3O_{12}$ film. The experimental data points (circles) are fitted to a Shirley background (dot-dot-dash line) and two Voigt components associated with an unscreened plasmon satellite (dash line) to high binding energy and a screened main peak (dot-dash line) to low binding energy. The difference curve is shown as a line underneath the fitted data.

determined from a linear extrapolation was found to occur at an energy of 3.95 ± 0.10 eV (Fig. 9). To work back from the value of the gap E_{doped} for the doped material to derive a value for the allowed direct gap $E_{undoped}$ of nominally undoped $In_4Sn_3O_{12}$ we must correct for two effects due to doping

$$E_{undoped} = E_{doped} - E_F + E_R. \tag{9}$$

The first correction arises because occupation of the conduction band blocks transitions into states whose energy is lower than the Fermi energy E_F: as discussed above E_F lies 0.85 eV above the conduction-band minimum. The second correction E_R arises from shrinkage or renormalization of the separation between the top of the valence band and the bottom of the conduction band as a result of the degenerate doping itself. The renormalization E_R arises in part from screening of the mutual exchange and Coulomb interactions between conduction- and valence-band states and in part from direct Coulomb interactions between the free electrons in the conduction band and the impurity centers which lead to electronic doping. Band-gap renormalization in Sn-doped In_2O_3 (Ref. 20) and Al-doped ZnO (Ref. 27) has been treated semiempirically by Granqvist and co-workers. More recently Walsh *et al.*[18] have calculated band-gap renormalization in Sn-doped In_2O_3 as a function of carrier concentration using *ab initio* methods and we have used a value $E_R = 0.18$ eV derived from this work. We thus obtain an estimate of $E_{undoped}$ equal to $(3.95 - 0.85 + 0.18)$ eV, i.e., 3.3 ± 0.1 eV.

Our measurements set the direct optical gap of $In_4Sn_3O_{12}$ slightly lower in energy than the estimate of ~3.5 eV made in the earlier work of Minami *et al.*[6] although these authors did not take account of the conduction-band occupation. As a comparison the direct optical gaps of In_2O_3 and SnO_2 (Ref. 28) are reported to be 3.62 and 3.75 eV, respectively. The tailing in the absorption coefficient at lower energy indicates that weaker transitions occur before the onset of the stronger allowed direct transitions. This behavior is reproduced in the simulated spectrum although the calculated data show a weak peak rather than a tail. However the calculations did not take full account of phonon effects which will undoubtedly broaden the structure in the absorption spectrum.

C. X-ray photoemission spectra

The spectral profile (Fig. 10) of the In $3d_{5/2}$ core line in the x-ray photoemission spectrum of $In_4Sn_3O_{12}$ shows a degree of asymmetry reminiscent of Sn-doped In_2O_3 (Ref. 29) and Sb-doped SnO_2.[30] In the present context, we ignore the possibility of further contributions to the In core line shape arising from multiple plasmon excitation or the contributions of chemically shifted In states in the topmost ionic layer.[29,31] The asymmetry results from an unscreened plasmon satellite residing to the high binding-energy side of a screened main peak. In these dilute electron-gas materials, plasmon energies are typically less than 0.7 eV and plasmon satellites overlap with the core-level peak to give an asymmetric broadening of the spectral line shape.[30] The overall full width at half maximum of the In $3d_{5/2}$ peak was determined to be 1.5 eV. The In $3d_{5/2}$ core line spectra (Fig. 10) were fitted with two Voigt components corresponding to a screened main peak to low binding energy and an unscreened plasmon satellite to high binding energy. The model consisting of two Voigt components gave an excellent fit to the spectral data and the addition of further components did not significantly improve the fit. The plasmon satellite accounts for approximately 70% of the overall spectral line shape. The intensity of the plasmon satellite and the fitted Lorentzian character observed in $In_4Sn_3O_{12}$ is intermediate between that of nominally undoped In_2O_3 and 4% doped ITO and is consistent with the observed carrier concentrations of these materials.[29] The high binding-energy satellite is much broader than the component at low binding energy and has greater Lorentzian character, typically ~60%, allowing for the distinctive tails at high and low binding energies to the overall spectrum. The

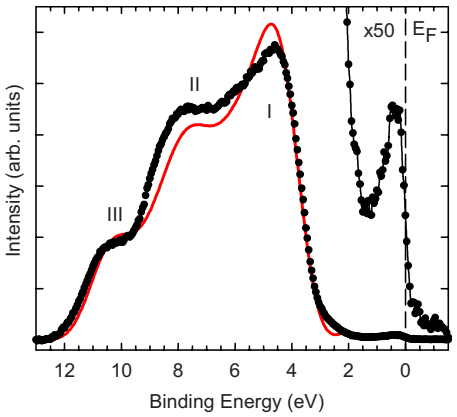

FIG. 11. (Color online) Valence-band photoemission spectrum of an $In_4Sn_3O_{12}$ film aligned to a weak feature arising from the occupation of conduction-band states after subtraction of a Shirley background. Distinct features of the valence band are labeled I–III. The position of the valence-band edge is determined by a linear extrapolation as 3.05 ± 0.10 eV. The cross-section weighted total DOS from the DFT calculations is shown as a solid line (red online) after convolution with a 0.8 eV broadening function. The broadened DOS has been normalized to the same maximum intensity as the experimental spectrum and is aligned to the first peak in the valence band.

splitting of the two components is found to be 0.46 eV which corresponds to the plasmon energy. From the plasmon energy, it is possible to determine the carrier concentration in the near surface region using the values of $\varepsilon_\infty = 4.57$ and $m^* = 0.26 m_e$ for the high-frequency dielectric constant and the effective mass as determined by the optical measurements. The measured plasmon energy of 0.46 eV for the $In_4Sn_3O_{12}$ film thus corresponds to a carrier concentration of 1.85×10^{20} cm^{-3} in the near surface region.

In Fig. 11 we show the valence-band structure of $In_4Sn_3O_{12}$ which is composed of three distinct features as predicted in the calculated density of states. As a comparison we also show the total DOS derived from the DFT calculations after convolution with a Gaussian function to allow for the broadening associated with phonons and the instrumental function of the spectrometer. As shown in Fig. 11, the features of the theoretical valence band match well with those of the experimental photoemission spectrum. Furthermore, by making a comparison with the calculated partial DOS presented above, it is possible to assign orbital character to the experimental band structure. Feature III at the bottom end of the valence-band spectrum corresponds to O $2p$ states strongly hybridized with Sn $5s$ and In $5s$ states. It can be seen in Fig. 3 that, in fact, the Sn $5s$ contribution to the valence band is comparable to the contribution to the conduction band due to very pronounced covalency. For the In $5s$ states the conduction-band contribution is, however, weaker than the valence-band contribution. The states of dominant O $2p$ character at the top of the valence band weakly hybridized with Sn $5d$ and In $5d$ states correspond to feature I in the photoelectron spectrum above (Fig. 11). The intermediate peak II corresponds to states again of dominant O $2p$ character but mixed with Sn $5p$ and In $5p$ states.

Taking the linear portion of the valence-band edge and extrapolating to the intercept gives an estimate of the position of the valence-band edge as 3.05 ± 0.1 eV. Since all binding energies are referenced to the Fermi level (shown in Fig. 11 as a dotted line), the presence of occupied states in the conduction band shifts the valence-band edge to higher binding energies. From the surface carrier concentration and effective mass, the position of the Fermi level with respect to conduction-band minimum, is calculated from a simple free-electron model as 0.45 eV. Inspection of the magnified ($\times 50$) valence-band edge shown in Fig. 11 reveals the conduction band as a weak but well-defined feature with a width of the order of 0.5 eV.

Following Walsh *et al.*,[18] at the free-electron concentration of 1.85×10^{20} cm^{-3}, the band-gap renormalization due to electron-electron and electron-impurity interactions is estimated as 0.11 eV. The electronic band gap of $In_4Sn_3O_{12}$ can then be calculated from the difference in energy of the valence-band onset (E_{VBE}) and the width of conduction band (E_F) subject to the renormalization (E_R) of the band gap at the observed carrier concentration

$$E_g = E_{VBE} - E_F + E_R. \tag{10}$$

The fundamental gap of $In_4Sn_3O_{12}$ is calculated in this way to be 2.7 ± 0.1 eV and lies very close to the reported band gap of 2.7 eV for In_2O_3 determined from valence-band photoemission measurements.[10,29,32] Equation (10) is clearly similar to Eq. (9) but we find a significant shift of 0.6 eV between the lowest energy gap as defined by photoemission experiments and the onset of strongly allowed optical absorption.

D. Surface-electron depletion

At this point, it is interesting to compare the carrier concentration of the bulk material determined from Hall measurements to that of the surface extracted from the x-ray photoemission spectra. Specifically, we find the surface-electron concentration is significantly less than that of the bulk material. Such a situation has also been observed in Sn-doped In_2O_3 and is rationalized from the position of the Fermi level with respect to that of the charge neutrality level (CNL).[33] In degenerately doped $In_4Sn_3O_{12}$ surface states with an energy determined by the position of the CNL must pin the Fermi level below that in the bulk. This results in a negative surface charge resulting from occupied acceptor states at the surface. Charge neutrality is then achieved by an upward bending of the bands relative to the Fermi level which results in a depletion of electrons at the surface. We can therefore surmise that the position of the charge neutrality level in $In_4Sn_3O_{12}$ must lie between Fermi levels of the surface and bulk, *i.e.*, in the range $0.45 \leq E_{CNL} \leq 0.85$ eV.

V. CONCLUDING REMARKS

The electronic structure of $In_4Sn_3O_{12}$ has been investigated by optical and x-ray photoemission spectroscopies and further compared to DFT calculations. We find the lowest electronic gap in $In_4Sn_3O_{12}$ of 2.7 eV is direct. Although

optical transitions near the band edges are not formally forbidden, they contribute low dipole intensity to the optical absorption spectrum. Thus the optical gap of $In_4Sn_3O_{12}$, determined here as 3.3 eV, lies significantly higher in energy ($\sim$0.6 eV) than the fundamental electronic band gap. It appears that the existence of weak-intensity transitions between the band extrema is a characteristic of In-O-derived systems. From the comparison of bulk and surface techniques, we have shown that surface-electron depletion occurs in $In_4Sn_3O_{12}$ with the CNL lying approximately 0.45–0.85 eV above the CBM. To conclude the existence of high electrical conductivity and optical transparency in $In_4Sn_3O_{12}$ is a result of a relatively low CBM with respect to the vacuum level combined with a relatively large fundamental band gap coupled with the fact that optical transitions originating from states close to the valence-band edge occur with weak intensity.

ACKNOWLEDGMENTS

The authors would like to thank J. S. Abell for access to and A. Bradshaw for technical assistance with the pulsed laser deposition facilities at the Department of Metallurgy and Materials, University of Birmingham. The National Centre for Electron Spectroscopy and Surface Analysis facility (Daresbury, U.K.) is supported by EPSRC under Grant No. EP/E025722/1. We are grateful to D. S. L. Law and G. Beamson for help with the XPS measurements. The experimental work on the transparent conducted oxides in Oxford was supported by Merck KGaA (Darmstadt).

*Corresponding author; david.oneil@chem.ox.ac.uk

[1] I. Hamberg and C. G. Granqvist, J. Appl. Phys. **60**, R123 (1986).
[2] C. G. Granqvist, Sol. Energy Mater. Sol. Cells **91**, 1529 (2007).
[3] T. Minami, Semicond. Sci. Technol. **20**, S35 (2005).
[4] J. L. Bates, C. W. Griffin, D. D. Marchant, and J. E. Garnier, Am. Ceram. Soc. Bull. **65**, 673 (1986).
[5] A. Ambrosini, G. B. Palmer, A. Maignan, K. R. Poeppelmeier, M. A. Lane, P. Brazis, C. R. Kannewurf, T. Hogan, and T. O. Mason, Chem. Mater. **14**, 52 (2002).
[6] T. Minami, Y. Takeda, S. Takata, and T. Kakuma, Thin Solid Films **308**, 13 (1997).
[7] N. Nadaud, N. Lequeux, and M. Nanot, J. Solid State Chem. **135**, 140 (1998).
[8] J. Choisnet, L. Bizo, R. Retoux, S. Hebert, and B. Raveau, J. Solid State Chem. **177**, 3748 (2004).
[9] C. Y. Ren, S. H. Chiou, and J. Choisnet, J. Appl. Phys. **99**, 023706 (2006).
[10] A. Walsh, J. L. F. Da Silva, S.-H. Wei, C. Korber, A. Klein, L. F. J. Piper, A. DeMasi, K. E. Smith, G. Panaccione, P. Torelli, D. J. Payne, A. Bourlange, and R. G. Egdell, Phys. Rev. Lett. **100**, 167402 (2008).
[11] WVASE32, J. A. Wollam Co., B. Johs, C. Herzinger, and B. Guenther, 2004.
[12] G. Kresse and J. Furthmüller, Phys. Rev. B **54**, 11169 (1996).
[13] G. Kresse and J. Furthmüller, Comput. Mater. Sci. **6**, 15 (1996).
[14] J. P. Perdew, K. Burke, and M. Ernzerhof, Phys. Rev. Lett. **77**, 3865 (1996).
[15] P. E. Blöchl, Phys. Rev. B **50**, 17953 (1994).
[16] D. Segev and S.-H. Wei, Phys. Rev. B **71**, 125129 (2005).
[17] B. Adolph, J. Furthmüller, and F. Bechstedt, Phys. Rev. B **63**, 125108 (2001).
[18] A. Walsh, J. L. F. Da Silva, and S.-H. Wei, Phys. Rev. B **78**, 075211 (2008).
[19] Z. C. Jin, I. Hamberg, and C. G. Granqvist, J. Appl. Phys. **64**, 5117 (1988).
[20] I. Hamberg, C. G. Granqvist, K. F. Berggren, B. E. Sernelius, and L. Engstrom, Phys. Rev. B **30**, 3240 (1984).
[21] F. Borondics, K. Kamaras, M. Nikolou, D. B. Tanner, Z. H. Chen, and A. G. Rinzler, Phys. Rev. B **74**, 045431 (2006).
[22] R. E. Dietz, M. Campagna, J. N. Chazalviel, and H. R. Shanks, Phys. Rev. B **17**, 3790 (1978).
[23] G. E. Jellison and F. A. Modine, Appl. Phys. Lett. **69**, 371 (1996).
[24] H. Fujiwara and M. Kondo, Phys. Rev. B **71**, 075109 (2005).
[25] T. Inaoka, D. M. Newns, and R. G. Egdell, Surf. Sci. **186**, 290 (1987).
[26] L. H. Hall, J. Bardeen, and F. J. Blatt, Phys. Rev. **95**, 559 (1954).
[27] B. E. Sernelius, K. F. Berggren, Z. C. Jin, I. Hamberg, and C. G. Granqvist, Phys. Rev. B **37**, 10244 (1988).
[28] V. T. Agekyan, Phys. Status Solidi A **43**, 11 (1977).
[29] V. Christou, M. Etchells, O. Renault, P. J. Dobson, O. V. Salata, G. Beamson, and R. G. Egdell, J. Appl. Phys. **88**, 5180 (2000).
[30] R. G. Egdell, T. J. Walker, and G. Beamson, J. Electron Spectrosc. Relat. Phenom. **128**, 59 (2003).
[31] R. G. Egdell, J. Rebane, T. J. Walker, and D. S. L. Law, Phys. Rev. B **59**, 1792 (1999).
[32] A. Bourlange, D. J. Payne, R. G. Egdell, J. S. Foord, P. P. Edwards, M. O. Jones, A. Schertel, P. J. Dobson, and J. L. Hutchison, Appl. Phys. Lett. **92**, 092117 (2008).
[33] P. D. C. King, T. D. Veal, D. J. Payne, A. Bourlange, R. G. Egdell, and C. F. McConville, Phys. Rev. Lett. **101**, 116808 (2008).